J Sol-Gel Sci Techn (2007) 42:79–88
DOI 10.1007/s10971-006-1517-3

Sol-gel modified Pechini method for obtaining nanocrystalline $KRE(WO_4)_2$ (RE = Gd and Yb)

M. Galceran · M. C. Pujol · M. Aguiló · F. Díaz

Received: 23 August 2006 / Accepted: 22 November 2006 / Published online: 1 January 2007

Abstract $KRE(WO_4)_2$ (RE = Gd and Yb) nanocrystalline powder was obtained by the modified sol-gel Pechini method. The precursor powder was calcined between 923 and 1023 K for a maximum of 6 h at air atmosphere. DTA-TG of the precursor powder shows that the temperature for total calcination is around 800–850 K. Molar ratio between the complexing agent and the metal ions in the first step of the method and molar ratio between the complexing agent and the ethylene glycol in the second step of the method were studied to optimize the preparation process. X-ray diffraction and IR spectroscopy were used to study the transformation from precursor powder into a crystalline monoclinic phase. Raman spectroscopy was used to study the vibrational structure of the nanoparticles. The Scherrer formula was used to confirm the grain sizes visualized by SEM and TEM techniques. Small nanoparticles in the range of 20–50 nm of monoclinic KREW have been successfully obtained by this methodology.

Keywords Sol-gel method · Monoclinic double tungstates · Nanocrystals · Ytterbium

M. Galceran · M. C. Pujol (✉) · M. Aguiló · F. Díaz
Física i Cristal · lografia de Materials (FiCMA), Universitat Rovira i Virgili, Campus Sescelades c/ Marcel.lí Domingo, s/n E-43007-Tarragona, Spain
e-mail: mariacinta.pujol@urv.cat

M. Galceran
e-mail: montserrat.galceran@estudiants.urv.cat

M. Aguiló
e-mail: magdalena.aguilo@urv.cat

F. Díaz
e-mail: f.diaz@urv.cat

1 Introduction

In recent years $KRE(WO_4)_2$ (RE = Gd and Yb) has been reported in the literature as a promising solid state laser material [1]. Ytterbium-doped tungstates are an interesting alternative to Nd:YAG applications [2]. The monoclinic phase of these materials has an interesting anisotropy in optical applications for obtaining polarized emissions. These materials are also known for their high value of the χ^3 third-order nonlinear coefficient, which makes them highly efficient materials for Stimulated Raman Scattering (SRS) applications [3, 4]. Moreover, KREW materials can be highly doped with active laser rare earth ions while maintaining their high crystalline quality and excellent properties. Examples of these materials are KYbW [5], KErW [6], KHoW [7] and KDyW [8].

To expand their applications, several preparations of these materials have been made. KREW bulk crystals were traditionally prepared by the Top Seeded Solution Growth Slow Cooling method (TSSG-SC). Thin films have been synthesized by laser ablation [9] and by Liquid Phase Epitaxial growth [10, 11] for waveguide and thin disk applications, respectively. To our knowledge, monoclinic KREW (RE = Gd and Yb) tungstates have not been prepared as nanocrystals.

Ceramic and nanocrystalline materials provide several alternatives to classic bulk laser crystals. YAG ceramic lasers have comparable optical properties to those of bulk laser crystals. In recent years, the output power of these laser ceramics doped with Nd has increased to the kW range [12]. Mechanical and thermal properties can be improved in a ceramic configuration for a laser [13]. As is mentioned in the literature, laser ceramics can be obtained in big size and cheaper than single crystal materials. The preparation of ceramic anisotropic materials for laser applications currently presents a challenge.

Sol-gel technology, by which composite organic-inorganic materials are made at relatively low temperature, involves the hydrolysis of the constituent molecular precursors and subsequent polycondensation to glass-like form [14]. Sol-gel methods enable homogenous samples to be obtained at low temperatures and the starting cationic composition to be maintained by using metal salts as raw materials and mixing them in a liquid solution. The most obvious advantage of this Sol-gel method is that reagents are mostly mixed in atomic level, which may increase the reaction rate and decrease the synthesis temperature. In 1967, Pechini [15] developed a process for the preparation of the precursor polymeric resin. First, a mixture of cations is formed in an organic *c*omplexing *a*gent, *CA*, (citric acid or ethylenediaminetetraacetic acid, EDTA) and ethylene glycol solution. Second, the cations become a chelate and the polymeric resin forms. Finally this polymer decomposes at 573 K. Two reactions are involved—a complex formation between citric acid or EDTA and metals, and a sterification between citric acid or EDTA and ethylene glycol (EG). The aim of the polymeric organic net by sterification is to reduce any segregation of the cations [16].

Nanostructured Yb:YAG materials were obtained by the Pechini method by Hreniak et al. [17]. In 2004 year, a thin film of $Gd_2(WO_4)_3$ was prepared using the Pechini method [18].

To our knowledge, KREW (RE = Gd and Yb) have not been obtained as nanoparticle powder. As we mentioned above, the preparation of ceramic anisotropic materials for laser applications is currently a challenge. With this in mind, the first step to creating an anisotropic laser ceramic of KREW, a well-known anisotropic solid state laser host, is to obtain monoclinic nanocrystals of KREW tungstates. The activity of the grains in the sintering process is known to be enhanced by the nature of nanodimensions [19]. Hence the importance of obtaining nanocrystals of KREW, which is the main objective of the present paper.

2 Experimental section

2.1 Preparation of the precursor polymeric resin

Powders of K_2CO_3 (Fluka, 99.0%), RE_2O_3 (Aldrich, 99.9%) and ammonium (para)tungstate $(NH_4)_{10}W_{12}O_{41}\cdot 7H_2O$ (Riedel-de Häen, 99%) were used as starting materials. They were dissolved in concentrated HNO_3. As WO_3 is insoluble in HNO_3 at room temperature, we used ammonium (para)tungstate. Afterwards, the nitrate solution was totally evaporated maintaining the solution around 100°C. Throughout this step, the elements were mixed atomically.

Taking in account the moles of the complexing agent [CA], the moles of the metal cations [METAL], and the moles of ethylene glycol [EG], two molar ratios: [CA]/[METAL] = C_M and [CA]/[EG] = C_E can be defined. The microstructure of the resulting powder is related with these two ratios. C_M describes the degree of the chelation process of the metal in the organic product. For solutions with low C_M ratios ($C_M < 1$), there may be precipitation of the metals salts on the solution and, therefore, no uniformity in the chelation of the metals. This is due to insufficient organic molecules to chelate metal cations. Two organic compounds were used as chelating agents: concentrated citric acid solution in the first experiment and EDTA, for the following experiments. With one molecule of citric acid, one metal ion can be chelated by three bonds, and with one molecule of EDTA, it can be chelated by six bonds. So EDTA has a stronger chelating power to metal ions than citric acid. On the other hand, for relatively high C_M ratios, it is easy to dissolve the metal ions but the amount of organics to be removed is excessive [20]. Then, in this paper we have studied the effect of C_M ratio in the range of C_M = 1, 2 and 3. Higher C_M ratios will lead to an excess of organics.

C_E describes the degree of sterification between the chelating agent and the ethylene glycol. This created a rigid polyester net that reduces any segregation of metals during the polymer decomposition process at high temperatures [21]. The ratio C_E affects morphologies in the ceramic powder. Equimolar ratio leads to the most porous resin [22, 23]. As well the studied range of C_E was C_E = 1, 2 and 3.

In this study, we used different C_M and C_E ratios in order to optimize them and study their effects. The precipitate was then dissolved in concentrated citric solution (99.9%) or concentrated EDTA solution (99.9%), governed by the C_M ratio. We then added ethylene glycol to produce a sterification, governed by the C_E ratio. The resin formation takes place at 363 K; during this reaction the resin gels. Afterwards, going on with the heating, the resin is dried.

2.2 Preparation of the nanocrystals

The following step was a previous calcination at 573 K during three hours to start to decompose the resin. The next step was to calcine the precursor powder, which is a brown powder, at different temperatures and at air atmosphere for several hours. Table 1 shows the conditions for these experiments. Experiments *1 to 3* were done to prepare KGdW; experiments *4 to 15* were done to prepare KYbW. From the *1*, *4*, *5*, 6 and *7*, at fixed C_M at C_E ratios, we determined the optimum calcination temperature and time. Further experiments were carried out to study the effects of the various C_M and C_E.

2.3 Experimental details and apparatus

Thermogravimetric thermal analysis (TA instruments DTA-TG device) of the precursor powder (approximately 10 mg)

Table 1 Summary of the experiments (C_M = [CA]/[METAL] and C_E = [CA]/[EG]). (*In this experiment the complexing agent, CA, was citric acid)

		Molar ratios		Calcination program				
					Calcination time			
Experiment	Compound	C_M	C_E	Calcination temperature (K)	t_1	t_2	t_3	t_4
1	KGdW	3*	2		573–1123 K (6–8 h) Fig. 4(a)			
2	KGdW	3	2	973	6			
3	KGdW	3	2	973	6			
4	KYbW	3	2	873	3 h	4 h	5 h	
5	KYbW	3	2	923	3 h	4 h	5 h	
6	KYbW	3	2	973	2 h	3 h	4 h	5 h
7	KYbW	3	2	1023	2 h	3 h	4 h	5 h
8	KYbW	3	1	973	30’	1 h30’	2 h	3 h
9	KYbW	3	3	973	30’	1 h30’	2 h	3 h
10	KYbW	1	2	973	2 h	3 h	4 h	5 h
11	KYbW	2	2	973	3 h	4 h	5 h	
12	KYbW	1	1	973	2 h	3 h	4 h	5 h
13	KYbW	1	3	973	3 h	4 h	5 h	6 h
14	KYbW	2	3	973	3 h	4 h	5 h	6 h
15	KYbW	2	1	973	3 h	4 h	5 h	6 h

was conducted using a DTA-TG instrument in an air flow of 90 cm^3/h at a heating rate of 10 K/min in order to characterize the thermal decomposition. Al_2O_3 was used as a reference.

Precursor powder and calcined powder at various stages of the calcination process were characterized by Fourier Transform Infrared Spectroscopy (FTIR) at room temperature with an FT/IR-680 Plus Fourier Transform Infrared Spectrometer by averaging 32 scans and with a resolution of 4 cm^{-1} for each spectrum.

Structural characterization was carried out by powder X-ray diffraction (XRD) using a D-5000 diffractometer, with a Bragg-Brentano parafocusing geometry, from Siemens with θ-θ configuration. This device contained an X-ray standard Cu-tube, so the radiation used was $K\alpha_1$ (λ_1 = 1.540560 Å). The detector was a double collimated scintillation counter. The measurements were carried out in step-scanning mode. The diffraction angle (2θ) ranged between 10 and 70°. The X-ray powder diffraction patterns were recorded at step size = 0.05°, step time = 3 s for identification of the crystalline phases and at step size = 0.02°, step time = 16 s for unit cell refinement. Lattice parameters were calculated using the FULLPROF program [24] based on the Rietveld method [25]. The number of refined parameters was 13. The single X-ray diffraction model was used as the starting structure [5, 26].

The crystallite size L, was measured using Scherrer's equation $L = K\lambda/(\beta cos\theta_B)$ for peak broadening due to size effects. β is the FWHM (Full width at half maximum) measured in radians on the 2θ scale, λ is the wavelength used, θ_B is the Bragg angle for the measured *hkl* peak and K is a constant equal to 0.9 for L taken as the volume-averaged crystallite dimension perpendicular to the *hkl* diffraction plane [27].

The scanning electronic microscope (SEM) JEOL JSM 6400 was used to observe the resulting KREW powder. The samples had to be coated by a conductor media, which is usually Au. The device used to sputter Au on our samples was Bal-Tec SCD004. SEM equipment was used to observe the degree of homogeneity of the samples through SEM micrographs. A transmission electron microscope (TEM) JEOL JEM-1011 with a MegaView III Soft Imaging System was also used to observe the nanoparticles of KREW. The images were observed using a current accelerating voltage of 90 kV.

Raman scattering was used to study the vibrational structure of the nanocrystals obtained. The experimental set-up comprised a Jobin-Yvon T64000 spectrometer with excitation in the visible via a CW argon laser (Coherent INNOVA 300, λ = 514 nm). Behind the triple monochromator (1800 g/mm), the light was detected by a two-dimensional CCD matrix cooled with liquid N_2. A premonochromator eliminated the plasma discharge lines of the argon laser. The laser power incident on the sample was about 2 mW. A backward scattering scheme was chosen to increase the signal-to-noise ratio.

Along the paper, some aspects of the nanocrystals were compared with a bulk single crystal of the monoclinic KREW obtained by Top Seeded Solution Growth, grown previously [5, 26].

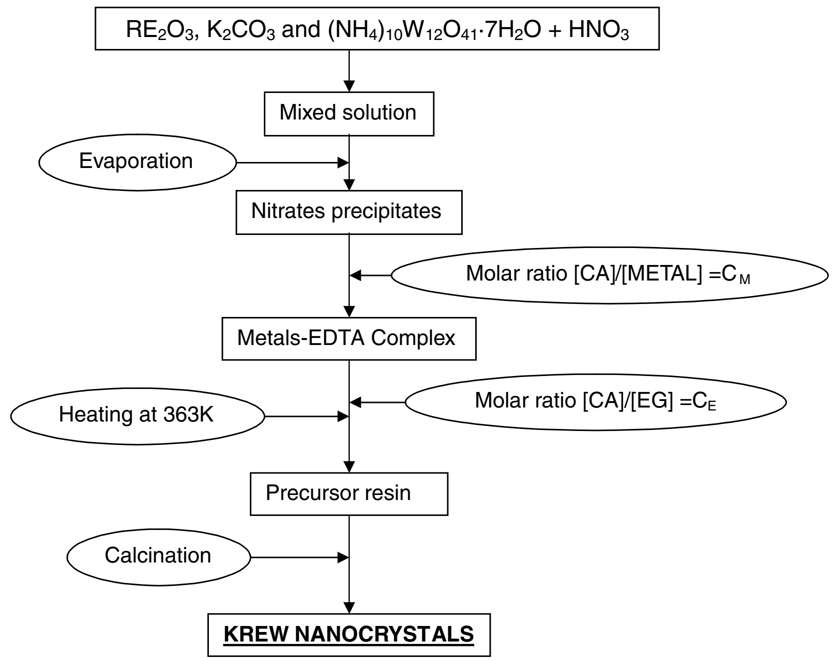

Fig. 1 Flow scheme of the Pechini method for KREW nanocrystals synthesis

3 Results and discussion

3.1 Applied modified Pechini method

A flow chart of the procedure for preparing the KREW using the modified Pechini method is shown in Fig. 1. The Pechini method uses the ability of organic acids to form polybasic acid chelated with several cations. Chelation, or the formation of complex ring-shaped compounds around the metal cations, then takes place in the solution. Citric acid or EDTA can be used as the chelating agent. Metals ions are chelated by the carboxyl groups and remain homogeneously distributed in the polymeric network.

The time and temperature of the calcination procedure affects the size of the grain. Powders prepared at the lowest temperature have the smallest crystallite size. At higher temperatures, the rates of crystal growth and molecular diffusion are enhanced, which fuses the small aggregated crystallites. This leads to the formation of well-defined crystals.

3.1.1 Control of modified Pechini method by DTA-TG measurements

The ethylenediaminetetraacetic acid (EDTA) (Fig. 2(a)) decomposes endothermically between 500 and 550 K in one step. The exothermic peak, which began around 780 K, represents the ignition of its derivatives. In the literature it is reported that pure ethylene glycol would present a strong endothermic peak at around 471 K, which represents the beginning of the boiling process [22, 28].

To determine how metallic cations affect the calcination process, precursor powders without metals were also prepared See Fig. 2(a) also for the DTA-TG curves. In all the DTA-TG curves studied, there are generally two weight losses. The first weight loss is attributed to the drying process up to 623 K—i.e. the removal of water. Also in this first step, it cannot be observed any peak attributed to the evaporation of ethylene glycol, which would be in excess. The average weight loss is 10–20%. As no peak at 550 K belonging to EDTA was observed, there was no EDTA in the precursor powder. The next, and most significant, slope, related to a more exothermic reaction, reflects the decomposition/combustion of the polyester [29]. Polyester decomposition involves a gradual change in the coordination of the metallic cations of the COO– group from the bidentated to the monodentated complex [30, 31]. At about 700 K, a small exothermic peak (in DTA) is attributed to self burning. This is the decomposition of residual organics, probably carbonates, which are formed as intermediate products. As we mentioned above, the second exothermic broad peak at around 750–920 K corresponds to the decomposition/combustion of the polyester and reflects a weight loss of 50–60%.

The DTA curves for the KREW precursor powders (see Fig. 2(b)) showed only one peak of between 780–840 K corresponding to calcination and ignition. As the crystallization process involves no weight loss in TG curve and exothermic peak in DTA curve, we therefore have an overlapped process in this range temperature. When the molar ratio C_M dropped to 1, the temperature was around 780 K, which means that there was less organic material than at higher C_M. On the other hand, the peak for the calcination of

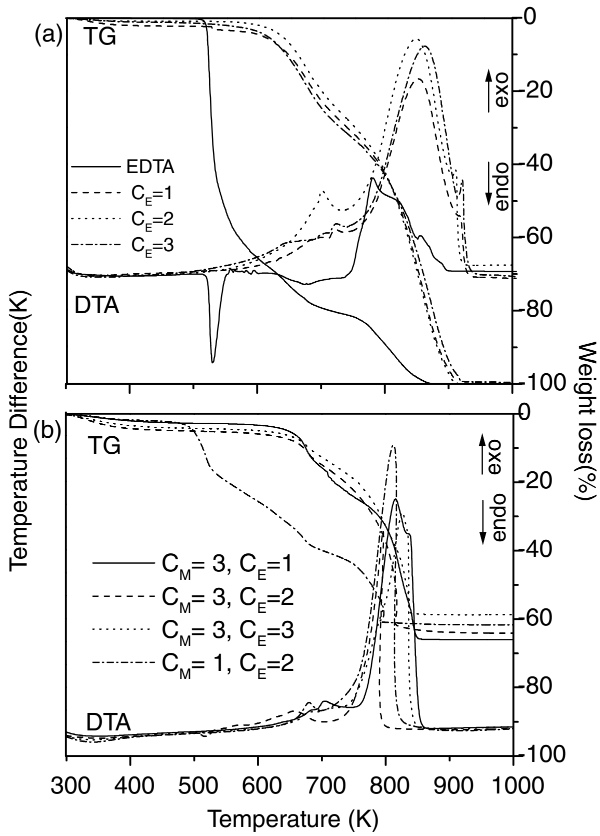

Fig. 2 DTA-TG analysis of EDTA and precursor powders (a) without metals, and (b) with metals

precursor powder without metallic cations appeared at higher temperatures (around 850 K) than precursor powders with metal cations. The presence of metal ions therefore had a catalytic effect on the pyrolysis of organics in the precursor powder [32]. The fact that the temperature of calcination is lower with metals and also decrease with the concentration of the metals means that the average temperature for producing nanocrystals is lower, so a lower cost of the synthesis procedure.

The overall weight loss was 60–70% of the initial weight. Weight loss increased when the molar ratio C_E decreased, which corresponded to an increase in the amount of organic material in the precursor powders. For example, when $C_E = 3$, the weight loss was around 59% and when $C_E = 1$ weight loss increased to 66%.

3.1.2 Control of modified Pechini method by IR spectroscopy

Infrared vibrational spectra of KREW powders and the precursor KREW powder at different steps of calcination are shown in Fig. 3. No significant differences were observed in any of the IR spectra from any experiment. The IR spectra of the experiment 10 is given as an example. The characteristic absorption lines of the infrared rays are useful for identifying the functional groups of the organic compounds. The band at 1640 cm^{-1}, which decreased during the calcination procedure, is attributed to hydroxyl groups (O–H). The vibrations of the carboxylic groups (–COO$^-$) were located at around 1726, 1400 and 1200 cm^{-1} and the bands at 1520 and 1400 cm^{-1} were assigned to the ionized carboxylates and carbonates [33]. These two groups of bands disappeared during the calcination process.

KREW formation is illustrated by the appearance of the typical bands of $(WO_4)^{2-}$ in the monoclinic KREW structures [34]. The inset in Fig. 3 shows the infrared vibrations that are characteristic of tungstates located at 925, 892, 820, 769 and 732 cm^{-1}. These peaks agree with those characterized by Macalik et al. [35]. A more detailed discussion of the vibrational structure of the nanocrystals of KREW is provided below.

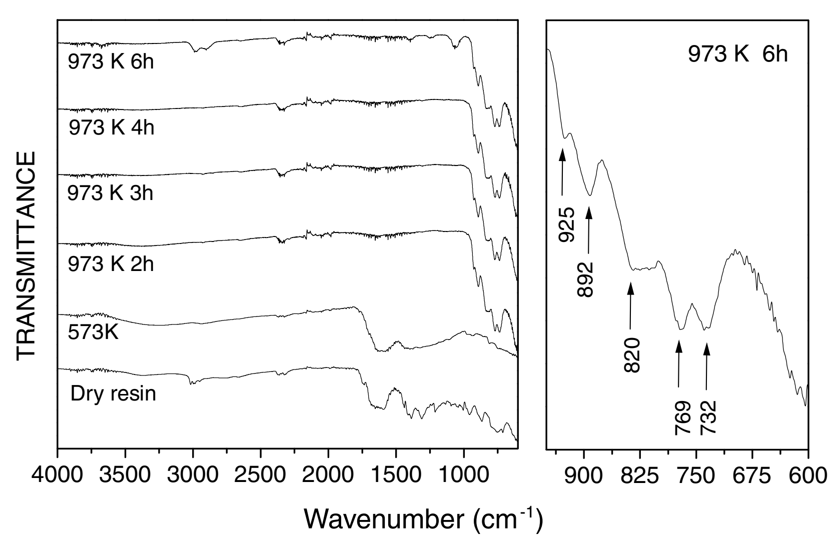

Fig. 3 IR spectra of the precursors powders at different calcinations times and of KYbW nanocrystals

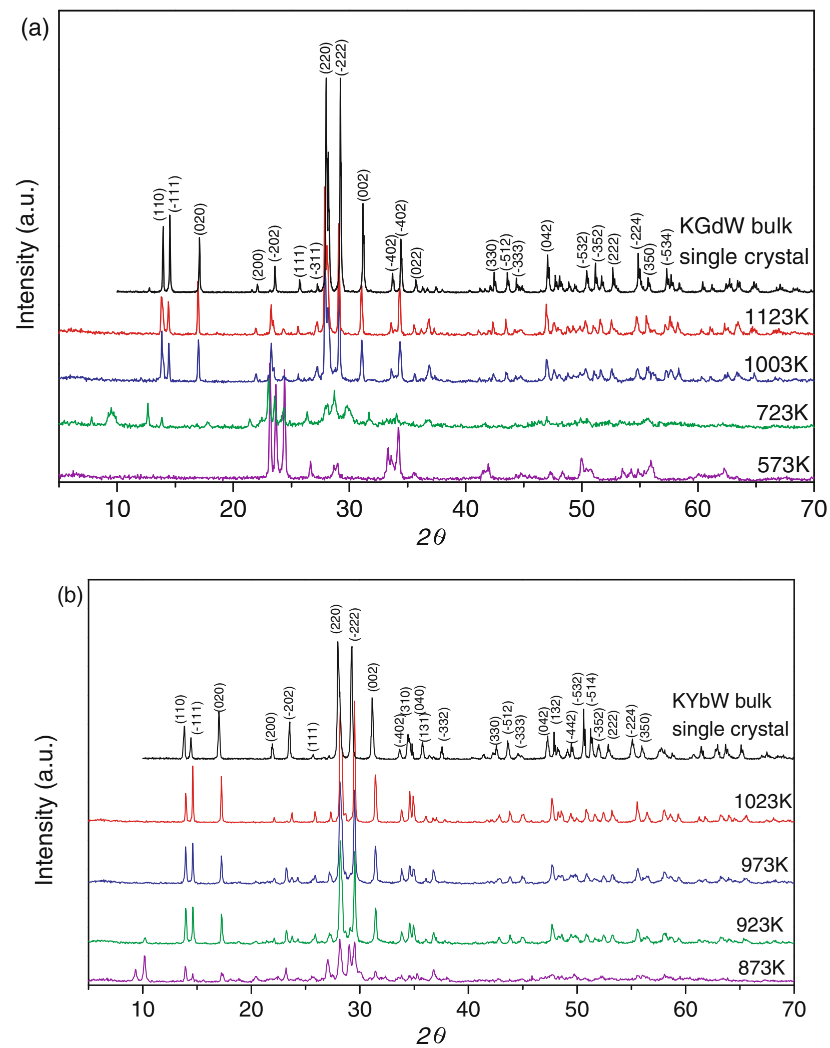

Fig. 4 X-ray powder diffraction of calcination procedure of precursor powder for (a) KGdW (b) KYbW

3.1.3 Control of modified Pechini method by X-Ray diffraction

To study the phase development as the calcination temperature and time increase, the precursor powder was calcined at air atmosphere and at various temperatures up to 1023 K. Crystalline phase analysis was then carried out using XRD. In Fig. 4(a), the X-Ray powder diffraction pattern at 573 K correspond to WO_3 and still at this low temperature no other crystalline phase is formed. At 723 K peaks of KGdW monoclinic phase start to appear and the rest of the peaks correspond to a mixture of oxide compounds, which can not be identified. So this calcination temperature is still low to achieve a complete crystallization of monoclinic KGdW. According to this approach, the optimum calcination temperature must be between 723 K and 1003 K. Figure 4(b) shows X-Ray powder diffraction patterns of the calcination of the KYbW nanopowders in smaller intervals of temperature than in Fig. 4(a). At 873 K, the peaks of KYbW monoclinic phase start to appear and some other peaks also indicate the presence of a mixture of oxide compounds not identified. At around 923 K, the X-Ray KREW powder diffraction pattern corresponds to the monoclinic phase and the shape of the peaks indicates a good crystallization. We can see that the crystallinity of the nanocrystals improves when the calcination temperature increases. On the other hand, an increase in calcination temperature led to an increase in the size of the nanoparticles. Figure 5 shows the SEM photographs of the nanopowders at 973 K and 1023 K. The optimum calcination temperature is therefore 973 K. The particles present an irregular shape, with rather size uniformity and tend towards aggregation.

3.2 Influence of the ratios C_M and C_E

We also analyzed the effects of the different C_M and C_E ratios. Figure 6 shows the particles at $C_M = 2, C_E = 2; C_M = 1, C_E = 2; C_M = 2, C_E = 3$ and $C_M = 2, C_E = 1$. A lower C_M ratio led to smaller KYbW nanoparticles. However, changing C_E did not influence the final size of the KREW particles very

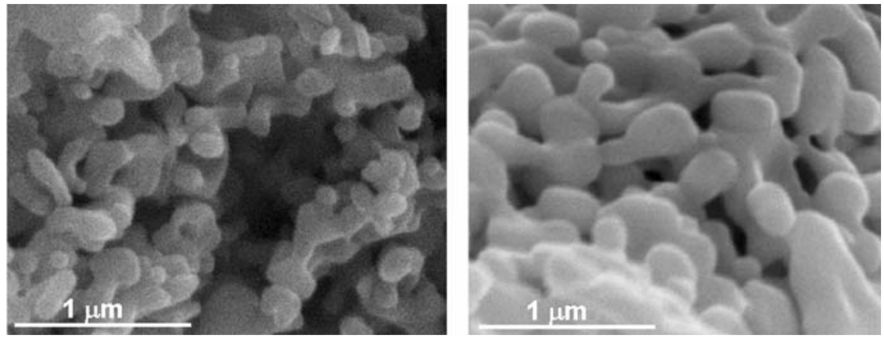

Fig. 5 SEM images of KYbW nanoparticles with $C_M = 3$ and $C_E = 2$. On the left, the calcination temperature was 973 K for 5 h and on the right, 1023 K for 5 h

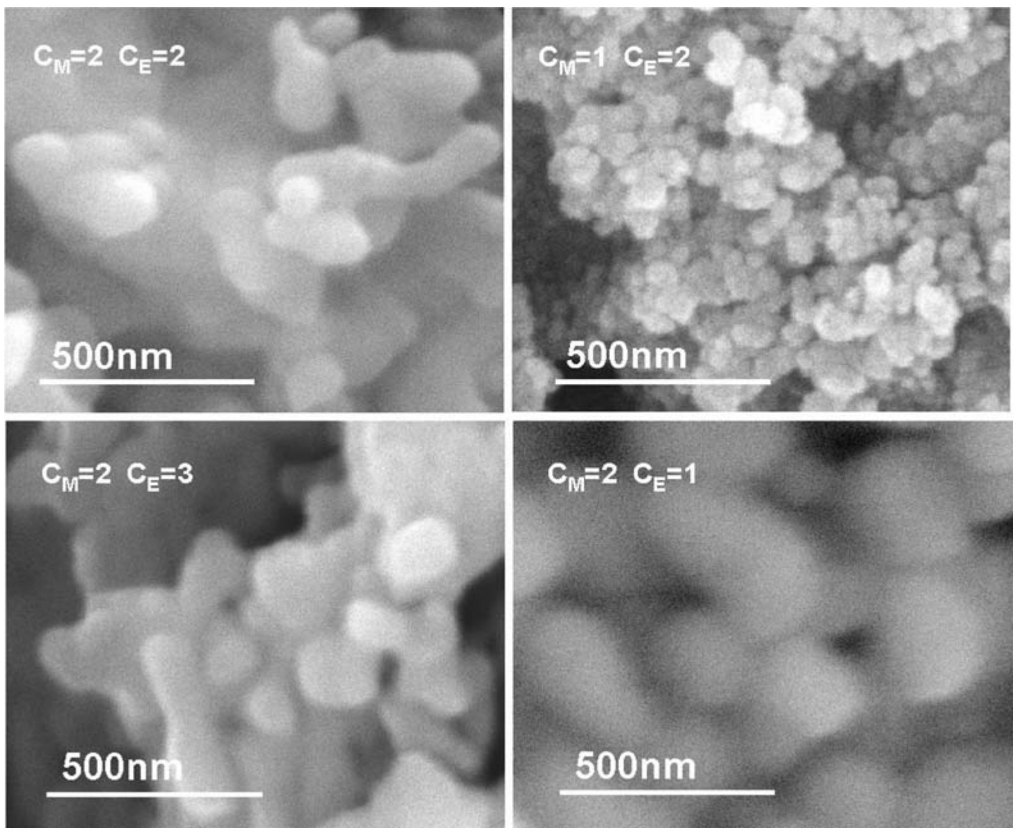

Fig. 6 SEM images of KYbW nanoparticles at different C_M and C_E ratios. The calcination temperature was 973 K for 3 h

much. These results show that $C_M = 1$ and $C_E = 2$ led to the smallest and most homogeneous particles.

Finally, Fig. 7 shows some KGdW nanoparticles ($C_M = 3, C_E = 2, T = 973$ K) and some KYbW nanoparticles ($C_M = 1, C_E = 2, T = 973$ K) observed by TEM microscopy. As we can see, the average size grain in these nanocrystals was 50–20 nm.

3.3 Structural study of the nanocrystals KREW

Figure 4 shows that the final crystalline structure of the powder belonged to the monoclinic system, which is the phase of interest for laser applications. This is important due to the fact that KREW (RE = Gd and Yb) present polymorphism in function of the temperature [36]. Refinement of the structure provided the unit cell parameters shown in Table 2. The crystal structure of monoclinic $KGd(WO_4)_2$ and $KYb(WO_4)_2$ bulk single crystals was refined at room temperature by using single crystal X-ray diffraction data as the starting model. The unit cell parameters were a = 10.6851(6) Å, b = 10.4327(6) Å, c = 7.5986(4) Å, $\beta = 130.770(3)^\circ$ and Z = 4 for KGdW (refinement reliability factor $R_{bragg} = 14.6$), and a = 10.6026(6) Å, b = 10.2597(6) Å, c = 7.5036(4) Å, $\beta = 130.753(3)^\circ$ and Z = 4 for KYbW (refinement reliability factor $R_{bragg} = 9.81$), both with the space group C2/c. Oxides with smaller mean particle sizes usually have larger

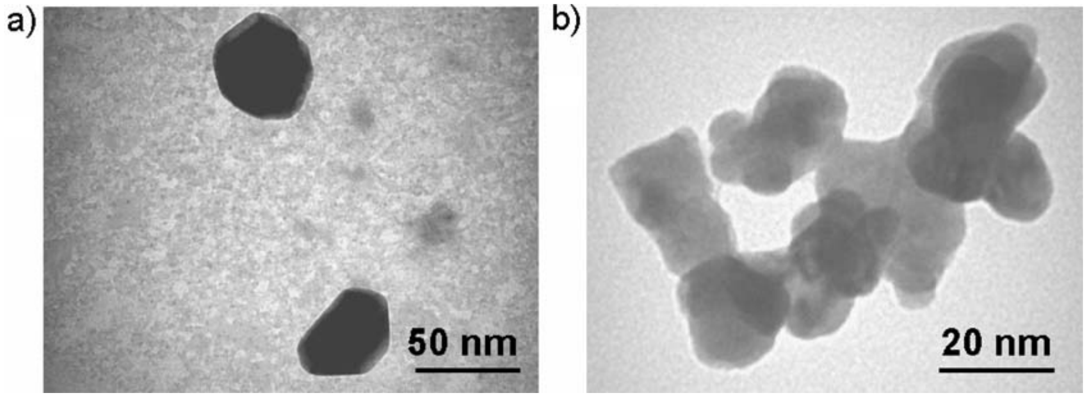

Fig. 7 TEM photographs of (a) KGdW ($C_M = 3, C_E = 2, T = 973$ K) and (b) KYbW ($C_M = 1, C_E = 2, T = 973$ K) nanoparticles

lattice parameters due to the creation of oxygen vacancies [16]. In our case, as the unit cell parameters were very similar to those refined for bulk single crystal samples (slightly smaller ***b*** unit cell parameter), this effect was not observed.

In nanocrystals, some physical properties are size-dependent [37, 38]. It is therefore very important to determine the crystal size. The Scherrer formula is based in the assumption that the diffraction peak is associated with a family of crystal planes in a size-limited crystal. The crystallite size, L, was measured using Scherrer's equation described above. The validity of the Scherrer formula has also been widely discussed in the literature. As it is valid only for small particles < 500 nm [27], we used the results as an estimation. These results are also shown in Table 2. These calculated values are slightly larger than the values of size grain observed by TEM (Fig. 7); the discrepancy among these values is originated to the fact that the values obtained by X-Ray diffraction come from an average measurement.

3.4 Vibrational study of KREW nanoparticles

Raman spectra of the nanocrystals can present differences in comparison to the bulk single crystal spectra, like the effects of optical phonon confinement in the nanocrystals due to the small size of the grains [39]. Moreover, the phonon energies of KREW provide important information for understanding the vibronic interactions of ytterbium in this material. As we have already mentioned, KREW crystallizes in the monoclinic space group C2/c with Z = 4. The unit cell is built from $[W_2O_8]^{-4}$ double chain of oxygen octahedra along ***c*** direction. Eight tungsten atoms are located in the C_1 positions [5, 26].

The 72 vibrational modes are distributed among the following irreducible representation: $N = 17\ A_g + 19\ B_g + 17\ A_u + 19\ B_u$. A_g and B_g modes are Raman active and A_u and B_u are infrared active modes. The optical modes can be further subdivided into translational ($T = 1A_u + 2B_u$ and T' $= 2A_g + 4B_g + 4A_u + 5B_u$), rotational ($L = 3A_g + 3B_g$) and internal (int $= 12A_g + 12B_g + 12A_u + 12B_u$) modes of the crystal for the anions $[W_2O_8]^{-4}$ [35]. The values of the phonon energies were determined in KGdW and KYbW nanocrystals with Raman spectroscopy and FTIR (see Table 3). The labelling assignment of the peaks was done as in a previous analysis for KYbW bulk single crystal [40] following the original notation for $CaWO_4$ [41] and also, the labelling assignment used Macalik et al. in more recent papers [35, 42]. Figure 8 shows the Raman spectra recorded with KREW nanocrystals at room temperature in the 0 to 1200 cm^{-1} frequency range in comparison with unpolarised Raman spectra recorded with bulk single crystal KREW. The spectra exhibit a complicated structure with about 22 peaks. The structures below 260 cm^{-1} can be attributed to external

Table 2 Unit cell parameters of the KREW nanocrystals (KREW bulk single crystals as a reference)

	a (Å)	b(Å)	c(Å)	β (°)	V	Size grain (nm)
KGdW bulk single crystal *[26]	10.652(4)	10.374(6)	7.582(2)	130.8(2)	634.2(5)	–
KGdW bulk single crystal **[43]	10.6890(6)	10.4438(5)	7.6036(4)	130.771(3)	642.834	–
KGdW nanopowder **	10.6851(6)	10.4327(6)	7.5986(4)	130.770(3)	641.493(6)	90–100
KYbW bulk single crystal *[5]	10.590(4)	10.290(6)	7.478(2)	130.70(2)	617.8(5)	–
KYbW bulk single crystal**[43]	10.6003(12)	10.2673(12)	7.5066(8)	130.766 (6)	618.78(12)	–
KYbW nanopowder**	10.6026(6)	10.2597(6)	7.5036(4)	130.753(3)	618.33(6)	50–60

* By X-ray single crystal diffraction.

**By X-ray powder diffraction.

Table 3 Vibrational frequencies for KGdW and KYbW nanocrystals at room temperature

Assignment	ν(cm^{-1})KGdW	ν(cm^{-1})KYbW
$T'(W^{6+})/(\nu_3{}^{\circ} - \nu_3{}^{-})$	78	66
$T'(W^{6+})/B_g$	86	87
$L(WO_6)^{*}\delta(WOW)/E_g$	113	113
$\gamma(WOOW)^{*}T'(K^{+})$	122	
$\gamma(WOOW)^{*}T'(K^{+})/\ E_u/\nu_1 - \nu_3{}^{\circ}$	148	148
$\gamma(WOOW)^{*}T'(K^{+})/\ A_u$	172	175
$T'(Gd^{3+})$	206	
$T'(Yb^{3+})/E_g$		218
$T'(K^{+})/B_g$	236	236
$T'(K^{+})$	261	260
$\delta(WOOW)$		288
$\delta(WOOW)$		299
γ (WOW) $/\nu_2{}^{-}$	313	318
$\delta(W-O)\ /\nu_2{}^{+}$	344	345
$\delta(W-O)$	350	351
$\delta(W-O)$	372	
$\delta(W-O)$		380
$\nu(W-O)/\nu_4{}^{-}$	402	406
$\delta(WOW)$	438	
$\delta(WOW)/\nu_4{}^{\circ}$		449
$\nu(WOOW)/\nu_4{}^{+}$	530	533
$\nu(WOOW)^{*}\ \nu(W-O)/\nu_3{}^{-}$	685	687
$\nu(WOOW)^{*}\ \nu(W-O)$	746	
$\nu(WOOW)^{*}\ \nu(W-O)$	759	758
$\nu(WOOW)^{*}\ \nu(W-O)/\nu_3{}^{\circ}$	772	
$\nu(WOW)^{*}\ \nu(W-O)/\nu_3{}^{+}$	809	810
$\nu(W-O)/\nu_1$	903	908

ν: stretching modes, δ: bending modes, γ: out-of-plane modes, T': translational modes, L: rotational modes, *: coupling of the vibrations.

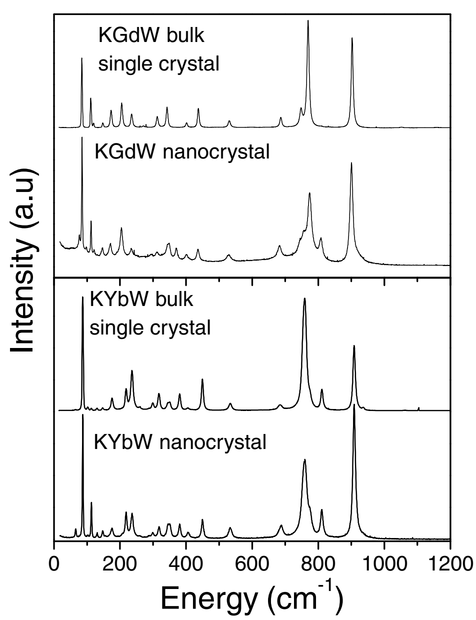

Fig. 8 Raman spectroscopy of KGdW and KYbW nanocrystals

lattice modes; e.g. translatory and rotational modes involving the heavy atoms of the unit cell. The ν_2 and ν_4 stretching modes appear in the 265–390 cm^{-1} region and the ν_1 and ν_3 bending modes in the 800–1100 cm^{-1} region. The bands in the 370–800 cm^{-1} region are related to the double oxygen bridge vibrations activated to increase the coordination number of tungsten from 4 to 6.

Table 4 Vibrational frequencies and linewidths of the spontaneous Raman peaks of KREW

KGdW nanocrystal		KGdW bulk single crystal	
Phonon energy (cm^{-1})	$\Delta\nu$(cm^{-1})	Phonon energy (cm^{-1})	$\Delta\nu$(cm^{-1})
86	2.4	84	3.0
772	12.5	769	7.0
903	8.7	902	6.54
KYbW nanocrystal		**KYbW bulk single crystal**	
Phonon energy (cm^{-1})	$\Delta\nu$(cm^{-1})	Phonon energy (cm^{-1})	$\Delta\nu$(cm^{-1})
87	2.5	90	3.8
758	18.2	763	14.6
908	9.13	911	8.4

The large cross section of the three peaks located at 86, 759 and 903 cm^{-1} for KGdW and 87, 758 and 908 cm^{-1} for KYbW makes KREW nanocrystals attractive for SRS applications. The Raman gain coefficient is linearly proportional to the scattering cross section and inversely proportional to the linewidth of the spontaneous Raman line [12]. The linewidth, $\Delta\nu$, of the three main peaks of KREWnanocrystals are showed in Table 4. Interestingly, in comparison with the Raman spectra of the bulk single crystals, the peaks with higher phonon energies have bigger linewidths and the peaks with lower phonon energies have smaller linewidths in the nanocrystals. We can see that the peak around 87 cm^{-1} has a promisingly low linewidth compared with those reported in the bibliography for YAG ceramic 5.7 cm^{-1}, sesquioxides ceramics Y_2O_3 4 cm^{-1} and Sc_2O_3 3.7 cm^{-1} [12].

4 Conclusions

The present paper reports the obtaining of the nanocrystals of the monoclinic KREW (RE = Gd and Yb) for first time up to now. Small nanocrystals in the 20–50 nm range were synthesized using the modified Pechini method. The working temperatures for this process are lower than the temperature for crystal growth of bulk single crystals of KREW (RE = Gd and Yb). The optimum range of calcination temperatures is 973 K and the optima molar ratios are $C_M = 1$ and $C_E = 2$. Also, the use of these ratios in the preparation process implies a reduction of the organic part to be eliminated.

The crystalline structure of the nanocrystals belonged to the monoclinic phase of these materials. Unit cell parameters were refined and were not significantly different from the bulk single crystals ones. Also, the vibrational structure of the KREW nanocrystals was very similar to the bulk single crystals till the studied level and the sharp linewidth of the most intense peaks in the spontaneous Raman spectra indicates that these are promising nanocrystals for SRS applications.

Acknowledgments We gratefully acknowledge financial support from CICyT under Projects MAT 2005-06354-C03-02, MAT2004-20471-E and CiT-020400-2005-14. This paper was also supported by EU-Commission Project DT-CRYS (STRP-NMP3-CT-2003-505580) and the Catalan Government under the project SGR2005-658. M. C. Pujol is supported by the Education and Science Ministry of Spain under Ramón y Cajal programme.

References

1. Kaminskii AA (1996) Crystalline lasers: Physical processes and operating schemes. CRC Press, New York
2. Krupke WF (2000) IEEE J Sel Top Quant Elec 6:1287
3. Ustimenko NS, Gulin AV (1998) Instrum Exp Tech 41:386
4. Lagatsky AA, Abdolvand A, Kuleshov NV (2000) Opt Lett 25:616
5. Pujol MC, Solé R, Massons J, Gavaldà Jna, Solans X, Díaz F, Aguiló M (2002) J Appl Crystallogr 35:108
6. Kaminskii AA, Pavlyuk AA, Butaeva TI, Bobovich LI, Lyubchenco VV (1979) Neorganicheskie Materialy 15:541
7. Majchrowski A, Borowiec MT, Michalski E, Zmija J, Dyakonov V, Szymczak H, Zayarnyuk T, Baranski M (2001) Cryst Res Technol 36:283
8. Borowiec MT, Dyakonov V, Fita I, Nabialek A, Pavlyuk A, Szewczyk A, Zaleski M, Zubov E (1999) J Magn Magn Mater 195:119
9. Okato T, Atanasov PA, Tomov RI, Obara M (2003) Appl Phys A Mater Sci Process 77:775
10. Griebner U, Liu J, Rivier S, Aznar A, Grunwald R, Solé RM, Aguiló M, Díaz F, Petrov V (2005) IEEE J Quant Elec 41:408
11. Aznar A, Solé RM, Aguiló M, Díaz F, Griebner U, Grunwald R, Petrov V (2004) Appl Phys Lett 85:4313
12. Kaminskii AA (2003) Phys Status Solidi A 200:215
13. Takaichi K, Yagi H, Shirakawa A, Ueda K, Hosokawa S, Yanagitani T, Kaminskii AA (2005) Phys Status Solidi A 1:R1
14. Reisfeld R, Jorgensen CK (1992) Optical properties of colorants or luminescent species in sol-gel glasses, Structure and bonding. Springer-Verlag, Heidelberg
15. Pechini MP (1967) US Patent No.3.330.697 July 1
16. Vaqueiro PP, Lopez-Quintela MA (1997) Chem Mater 9:2836
17. Hreniak D, Strek W, Mazur P, Pazik R, Zabkowska-Waclawek (2004) Opt Mater 26:117
18. Pang ML, Lin J, Yu M (2004) J Solid State Chem 177:2237
19. Stojanovic BD (2003) J Mater Process Technol 143:78
20. Roy S, Sigmund WW, Aldinger F (1999) J Mater Res 14:1524
21. Woon Kwon S, Bin Park S, Seo G, Tai Hwang S (1998) J Nucl Mater 257:172
22. Tai LW, Lessing PA (1992) J Mater Res 7:502
23. Laberty-Robert Ch, Ansart F, Deloget C, Gaudon M, Rousset A (2001) Mater Res Bull 36:2083
24. Rodriguez-Carvajal J (2000) Reference guide for the computer program fullprof. Laboratorie León Brillouin. CEA-CNRS. Saclay, France
25. Rietveld HM (1969) J Appl Crystallogr 2:65
26. Pujol MC, Solé R, Massons J, Gavaldà Jna, Solans X, Zaldo C, Díaz F, Aguiló M (2001) J Appl Crystallogr 34:1
27. Cullity BD (1978) Element of x-ray diffraction. Addison-Wesley
28. Interranta LV, Jiang Z, Larkin DJ (1998) ACS Symp Ser 77:168
29. Quinelato AL, Longo E, Perazolli LA, Varela JA (2000) J Eur Ceram Soc 20:1077
30. Cerqueira M, Nasar RS, Longo E, Leite ER, Varela JA (1995) Mater Lett 22:181
31. Fernández JDG, Melo DMA, Zinner LB, Salustiano CM, Silva ZR, Martinelli AE, Cerqueira M, Alves Junior C, Longo E, Benardi MIB (2002) Mater Lett 53:122
32. Agarwal V, Liu M (1997) J Mater Sci 32:619
33. Nakamoto K (1997) Infrared and Raman Spectra of inorganic and coordination compounds, 5th edn. Ed. Wiley-Interscience, New York
34. Hanuza J, Macalik L (1987) Spectrochim Acta A 43A:361
35. Macalik L, Hanuza J, Kaminskii AA (2002) J Raman Spectrosc 33:92
36. Klevtsov PV, Kozeeva LP, Kharchenko LP, Yu L, Pavlyuk AA (1974) Sov Phys-Crystallogr 20:342
37. Schoonman J (2000) Solid State Ionics 2135:5
38. Tissue BM (1998) Chem Mater 10:2837
39. Pokatilov EP, Klimin SN, Fomin VM, Devreese JT (2002) Phys Rev B 65:075316-1
40. Pujol MC, Bursukova MA, Guell F, Mateos X, Solé R, Gavaldà Jna, Aguiló M, Massons J, Díaz F, Klopp P, Griebner U, Petrov V (2002) Phys Rev B 65:165121
41. Porto SPS, Scott JF (1967) Phys Rev B 157:716
42. Macalik L, Deren PJ, Hanuza J, Strek W, Demidovich AA, Kuzmin AN (1998) J Mol Struct 450:179
43. Pujol MC, Mateos X, Solé R, Massons J, Gavaldà Jna, Díaz F, Aguiló M (2001) Mater Sci Forum 710:378–381